Molecular Neurobiology (2019) 56:3984–3998
https://doi.org/10.1007/s12035-018-1353-9

Visualization of the Breakdown of the Axonal Transport Machinery: a Comparative Ultrastructural and Immunohistochemical Approach

Sebastian Rühling[1] · Franziska Kramer[1] · Selina Schmutz[1] · Sandra Amor[2,3] · Zhan Jiangshan[1] · Christoph Schmitz[1] · Markus Kipp[1] · Tanja Hochstrasser[1]

Received: 25 June 2018 / Accepted: 13 September 2018 / Published online: 21 September 2018

Abstract

Axonal damage is a major factor contributing to disease progression in multiple sclerosis (MS) patients. On the histological level, acute axonal injury is most frequently analyzed by anti-amyloid precursor protein immunohistochemistry. To what extent this method truly detects axonal injury, and whether other proteins and organelles are as well subjected to axonal transport deficits in demyelinated tissues is not known. The aim of this study was to correlate ultrastructural morphology with the immunohistochemical appearance of acute axonal injury in a model of toxin-induced oligodendrocyte degeneration. C57BL/6J mice were intoxicated with 0.25% cuprizone to induce demyelination. The corpus callosum was investigated by serial block-face scanning electron microscopy (i.e., 3D EM), immunohistochemistry, and immunofluorescence microscopy. Brain tissues of progressive MS patients were included to test the relevance of our findings in mice for MS. Volumes of axonal swellings, determined by 3D EM, were comparable to volumes of axonal spheroids, determined by anti-APP immunofluorescence stains. Axonal swellings were present at myelinated and non-myelinated axonal internodes. Densities of amyloid precursor protein $(APP)^+$ spheroids were highest during active demyelination. Besides APP, vesicular glutamate transporter 1 and mitochondrial proteins accumulated at sites of axonal spheroids. Such accumulations were found as well in lesions of progressive MS patients. In this correlative ultrastructural-immunohistochemical study, we provide strong evidence that breakdown of the axonal transport machinery results in focal accumulations of mitochondria and different synaptic proteins. We provide new marker proteins to visualize acute axonal injury, which helps to further understand the complex nature of axonal damage in progressive MS.

Keywords Cuprizone · Axonal damage · APP · VGLUT1 · Mitochondria

Introduction

There is broad consensus that multiple sclerosis (MS) represents more than a purely inflammatory demyelinating disease. Most patients initially show with a relapsing-remitting (RR) course, which is usually followed by a secondary progressive phase [1]. These clinical phenotypes are thought to be associated with different underlying pathologies. While inflammatory lesions in the white matter are believed to be associated with the relapses during the RR disease stage, neuronal loss and axonal damage are widely considered to underlay the disease progression [2, 3]. Morphological changes of injured axons include focal axonal swellings, which are associated with impaired axonal transport of proteins and organelles. This impaired axonal transport machinery can be visualized by immunohistochemistry for accumulated proteins that are synthesized in the cell body and transported along the axon to their synaptic destination [4–7]. The most commonly used immunohistochemical marker to visualize axonal transport deficits is amyloid precursor protein (APP) [7]. APP is an integral glycoprotein type 1, which is transported to the axonal terminal via anterograde axonal transport [8]. There, APP is considered to regulate synaptic activity and stability [9, 10]. In case of a disturbed axonal transport machinery, APP accumulates at the side of axon injury and can then be visualized by immunohistochemistry as spheroids [11, 12]. Focal accumulation of APP is observed in MS lesions and

Electronic supplementary material The online version of this article (https://doi.org/10.1007/s12035-018-1353-9) contains supplementary material, which is available to authorized users.

✉ Tanja Hochstrasser
tanja.hochstrasser@med.uni-muenchen.de

[1] Department of Neuroanatomy, Ludwig-Maximilians-University of Munich, Pettenkoferstr. 11, 80336 Munich, Germany

[2] Department of Pathology, VU University Medical Center, Amsterdam, The Netherlands

[3] Blizard Institute, Barts and The London School of Medicine and Dentistry, Queen Mary University of London, London, UK

correlates with densities of macrophages and $CD8^+$ T lymphocytes within lesions [13, 14]. The accumulation of APP^+ spheroids has also been observed in animal models of MS, including the cuprizone model [15].

The cuprizone model is a model of toxic demyelination. Oral administration of cuprizone induces degeneration of oligodendrocytes, which is closely followed by microglia and astrocyte activation that ultimately leads to demyelination [16, 17]. After 5–6 weeks of cuprizone intoxication, the corpus callosum is almost completely demyelinated, a process called "acute demyelination." In contrast, prolonged cuprizone intoxication (> 12 weeks) leads to an impairment of oligodendrocyte regeneration and insufficient remyelination, termed "chronic demyelination" [18, 19]. Like in other preclinical MS animal models, in the cuprizone model, the number of APP^+ spheroids correlates to the extent of inflammatory lesion activity [20].

For the maintenance of neuronal health and function, vesicular transport is vital [21, 22]. Vesicular glutamate transporters (VGLUTs) and the vesicular gamma-aminobutyric acid (GABA) transporter (VGAT) are specifically expressed in cell bodies and axon terminals of excitatory glutamatergic or inhibitory GABAergic and glycinergic neurons, respectively. They are transported from the cell body to nerve terminals via anterograde axonal transport. Then, they selectively move glutamate or GABA/glycine from the cytoplasm into synaptic vesicles and contribute via this mechanism to the maintenance of cell homeostasis [23, 24]. VGLUT1 is principally associated with excitatory cortico-cortical projections [25], while VGAT is expressed by inhibitory neurons [24].

Balanced mitochondrial transport is important for the maintenance of axonal health. Most mitochondria are generated in the cell body and are transported along the microtubular network by microtubule-based motor proteins to areas with high energy demands. Once an axon loses its myelin sheath (i.e., demyelination), the demand for energy increases [26] with subsequent changes in activity and density of mitochondria in demyelinated areas [27, 28]. Increased mitochondrial density is important for axon regeneration [28]; however, there is accumulating evidence that focal accumulation of axonal mitochondria may as well contribute to axonal degeneration [29].

The aim of this study was to correlate ultrastructural morphology with the immunohistochemical presentation of acute axonal injury in a model of toxin-induced oligodendrocyte degeneration.

Materials and Methods

Animals and Induction of Demyelination

C57BL/6J mice (Janvier Labs, Le Genest-Saint-Isle, France) and hGFAP/EGFP transgenic mice [30] were kept under standard laboratory conditions according to the Federation of European Laboratory Animal Science Association's recommendations. All experimental procedures were approved by the Review Board for the Care of Animal Subjects of the district government (Upper Bavaria, Germany, 55.2-1-54-2532-73-15) and were performed according to international guidelines on the use of laboratory mice. Demyelination was induced by feeding male mice (19–21 g) with ground standard rodent chow containing 0.25% (*w*/*w*) cuprizone (bis-cyclohexanone oxaldihydrazone, Sigma-Aldrich Inc.). Cuprizone treatment was maintained for 1, 3, 5, or 12 weeks. Control mice were fed standard rodent chow.

MS Tissue

Autopsy samples of human brain material were obtained from the Netherlands Brain Bank and with the ethical approval of the VU University Medical Ethical Committee (Amsterdam, The Netherlands). Paraffin-embedded postmortem brain tissues were obtained through a rapid autopsy protocol from clinically and neuropathologically validated patients [31]. Studies were performed on postmortem human brain tissue from 4 MS cases (3 female, 1 male; 3 patients with SPMS, 1 patient with primary progressive MS). The ages of the patients ranged from 49 to 77 years. All patients had given written informed consent for autopsy and use of brain tissues for research purposes.

Immunohistochemistry (IHC) and Immunofluorescence

Mice were transcardially perfused with 3.7% paraformaldehyde in phosphate-buffered saline (PBS; pH 7.4). After overnight postfixation in the same fixative, brains were dissected, embedded in paraffin, and cut into 5-μm-thick coronal or sagittal sections. Some brains were cryoprotected in sucrose, and thereafter quickly frozen. The frozen brains were cut into 40-μm-thick coronal cryo-sections.

For immunohistochemistry, paraffin sections were deparaffinized, rehydrated, if necessary heat-unmasked in either citrate (pH 6.0) or Tris/EDTA-buffer (pH 9.0), and blocked with PBS containing 5% normal serum or a mixture of 2% normal serum, 0.1% cold water fish skin gelatin, 1% bovine serum albumin, and 0.05% Tween-20. Thereafter, slides were incubated overnight at 4 °C with the primary antibodies diluted in blocking solution. The following primary antibodies were used for mouse tissues: anti-myelin proteolipid protein (PLP; 1:5000, Bio-Rad; RRID:AB_2237198), anti-ionized calcium-binding adaptor molecule 1 (IBA1; 1:5000, Wako; RRID:AB_2665520), anti-glial fibrillary acidic protein (GFAP; 1:5000, Abcam; RRID:AB_304558), anti-amyloid precursor protein (APP; 1:5000; Merck Millipore;

RRID:AB_94882), anti-voltage-dependent anion-selective channel 1 (VDAC-1; 1:8000, Abcam; RRID:AB_443084), anti-cytochrome c oxidase subunit 4 (COX4; 1:500, Abcam; RRID:AB_445559), anti-vesicular glutamate transporter 1 (VGLUT1 1:2000; Abcam; RRID:AB_10710315), and anti-vesicular GABA amino acid transporter (VGAT; 1:1000, Thermo Fisher Scientific; RRID:AB_2637258). Sections were subsequently incubated with biotinylated secondary antibodies for 1 h at room temperature, followed by peroxidase-coupled avidin-biotin-complex (ABC kit; Vector Laboratories). The antigen-antibody conjugate was then visualized with 3,3′-diaminobenzidine (DAB; DAKO). Sections were counterstained with standard hematoxylin to visualize cell nuclei, if appropriate.

For immunofluorescence staining, slides were incubated with the following primary antibodies: anti-APP (1:5000), anti-VGLUT1 (1:2000), anti-adenomatous polyposis coli (APC, 1:200, Merck Millipore; RRID:AB_2057371), anti-IBA1 (1:2000), or anti-GFAP (1:5000) overnight at 4 °C. Sections were subsequently incubated with appropriate secondary antibodies (Alexa Fluor 488 or Alexa Fluor 594, 1:500, Invitrogen) for 2 h at room temperature and counterstained with 4′,6-diamidino-2-phenylindole (DAPI). Frozen sections were stained free-floating (APP; 1:200).

To visualize myelin and inflammatory infiltrates in human tissues, anti-PLP (1:5000) and anti-major histocompatibility complex class II (MHC-II (LN3); 1:1500, Thermo Fisher Scientific; RRID:AB_10979984) antibodies were used. Axonal damage was detected by anti-APP (1:100), anti-VGLUT1 (1:2000) and anti-COX4 (1:500) antibodies. Antigen-primary antibody conjugates were visualized using horseradish peroxidase-labeled linked polymer secondary antibodies (EnVision, Dako) and DAB as a peroxidase substrate. For immunofluorescence staining, human tissues were incubated with the following primary antibodies: anti-APP (1:50) and anti-VGLUT1 (1:500) overnight at room temperature. Sections were subsequently incubated with appropriate secondary antibodies (Alexa Fluor 488 or Alexa Fluor 594, 1:500, Invitrogen) for 2 h at room temperature and counterstained with DAPI.

Serial Block-Face Scanning Electron Microscopy

Myelinated and partially demyelinated (i.e., 3 weeks cuprizone intoxication) corporacallosa (CC) tissues were analyzed by serial block-face scanning electron microscopy (i.e., 3D EM). To this end, mice were perfused with 2.5% (wt/vol) glutaraldehyde and 3.7% paraformaldehyde, and tissue blocks containing the CC were removed, stained with heavy metals, and embedded in resin as previously described (Ohno et al. 2014). 3D EM was performed by using a SigmaVP scanning electron microscope (Carl Zeiss) equipped with a 3View in-chamber ultramicrotome system (Gatan, Pleasanton, CA, USA). Serial image sequences were generated at 80 nm steps, providing image stacks > 10-μm deep and 48-μm × 48-μm wide at a resolution of 5–10 nm per pixel. Images were processed with the software Reconstruct (BU, Boston, MA, USA) and BioVis3D (Montevideo, Uruguay). 3D EM was performed by Renovo Neural, Inc. (Cleveland, OH, USA).

Evaluation of Histological Parameters

A group of 3–8 animals was evaluated at each time point. The medial CC including the cingulum bundle (CB) was analyzed at the level R265 according to the online mouse brain atlas published by Sidman et al. (http://www.hms.harvard.edu/research/brain/atlas.html). Stained sections were analyzed using either a Nikon Eclipse 50i or an Olympus BX50 microscope. To determine levels of myelination, microgliosis, and astrocytosis in the region of interest (ROI), staining intensity was quantified using ImageJ (version 1.47v, NIH, Bethesda, MD, USA) as described previously [32, 33]. Staining intensities are given as percentage area of the entire ROI after binary conversion of the digital image. For quantification of APP^+, $VGLUT1^+$, $COX4^+$, and $VDAC1^+$ spheroid densities, particle densities of two consecutive sections per mouse were evaluated, averaged, and given as numbers of spheroids per mm^2. Spheroids were only counted if not localized around a cell nucleus. Additionally, the diameters of $VGLUT1^+$ and $COX4^+$ spheroids were measured using ImageJ after image calibration. For quantification of APP/VGLUT1 and APP/COX4 single and double positive spheroids, stained brain sections were digitalized, the CC outlined, and spheroids counted in a blinded approach using Stereo Investigator software (version 11, MBF Bioscience, Williston, VT, USA). Volume analysis of spheroids was done using 3D EM and confocal fluorescence image stacks. For fluorescence image stacks, serial image sequences from thick sections were generated at 200 nm steps using an Olympus BX51-Wi fluorescence microscope station and Stereo Investigator software. Images were processed and volumes of APP^+ spheroids ($n = 90$) were automatically measured with Neurolucida360 (version 2017.01.2, MBF Bioscience, Williston, VT, USA) and Neurolucida Explorer software (version 2017, MBF Bioscience). In 3D EM image stacks, the areas of axonal swellings ($n = 20$) were measured using ImageJ and the volume was calculated using the formula: total area × cutting thickness (≙ 80 nm). To compare the volumes of the two methods, the volume of cell nuclei was used as normalization value. The volume of cell nuclei was measured using Neurolucida360/Neurolucida Explorer ($n = 268$) and ImageJ ($n = 14$), respectively.

MS brain lesions were characterized by anti-MHC-II (LN3) and anti-PLP immunostainings as published previously [34]. To exclude autofluorescence of $APP^+/VGLUT1^+$ spheroids in MS lesions, double stained APP/VGLUT1 slides were compared with consecutive slides stained for APP only.

Statistical Analyses

All data are given as arithmetic means ± standard error of the mean (SEM). Differences between groups were statistically tested using GraphPad Prism 5 (version 5.04, GraphPad Software Inc., La Jolla, CA, USA). In all cases, the Kolmogorov-Smirnov test was applied to test for normal distribution. To compare two groups, the Mann-Whitney *U* test was used for non-parametric data. To compare more than two groups, data were analyzed by one-way or two-way analysis of variance (ANOVA) followed by Bonferroni or Dunnett's s multiple comparison post hoc test. For analysis of non-parametric data the Kruskal–Wallis-test followed by Dunn's post hoc test was used. p values ≤ 0.05 were considered to be statistically significant and are indicated by asterisks or hashtags (*#$p < 0.05$; **##$p < 0.01$; ***###$p < 0.001$).

Results

Demyelination and Glial Activation During Cuprizone-Induced Demyelination

We first investigated the myelination status and glial activation during the course of cuprizone-induced demyelination (Fig. 1). Densitometrical analysis of anti-PLP immunoreactivity revealed normal myelin in the middle part of the CC and the CB of control mice. Severe demyelination of the CC, but not of the CB, was present after 5 weeks (acute demyelination) and 12 weeks (chronic demyelination) of cuprizone treatment (Fig. 1a–c, j). After acute demyelination, there was extensive infiltration of IBA1$^+$ microglia and GFAP$^+$ astrocytes that altered tissue morphology and increased the CC area. On the morphological level, microglia had retracted processes and enlarged cell bodies. Astrocytes, as well, showed enlarged cell bodies and disorganized process distribution. Notably, after chronic demyelination, IBA1 immunoreactivity was attenuated while severe astrocytosis was still present (Fig. 1d–i, k, l).

Ultrastructural Axonal Swellings Have a Similar Volume as Immunohistochemical Spheroids

It was shown that the magnitude of impaired axonal transport of proteins and organelles correlates with the extent of inflammatory demyelination [6, 7]. This impaired axonal transport is usually detected by immunohistochemistry against APP. In line with previous results [15, 20], APP$^+$ spheroids were virtually absent in the CC of control animals (1.8 ± 1.3 APP$^+$ spheroids/mm^2; Fig. 2a), while profound accumulation of APP (454.3 ± 43.4 APP$^+$ spheroids/mm^2; $p < 0.001$ vs control) was detected after acute demyelination (5 weeks cuprizone) (Fig. 2b). APP$^+$ spheroids were still observable at week 12 (Fig. 2c), albeit to a lower extent (78.5 ± 14.5 APP$^+$ spheroids/mm^2; $p < 0.001$ vs control; $p < 0.01$ vs 5 weeks).

To further characterize axonal spheroids on the ultrastructural level, we performed 3D EM of the CC at week 3 and compared the ultrastructure with CC tissues isolated from control mice. Ultrastructural analysis revealed normal-shaped axons with intact myelin sheaths in control mice (Fig. 2d). In 3 weeks cuprizone-treated mice, axons were partly demyelinated and axonal swellings could be readily identified (Fig. 2e, f). Interestingly, we found axonal swellings affecting myelinated and demyelinated axonal internodes (Supplementary Fig.1).

Although it seems reasonable that the axonal swellings observed on the ultrastructural level represent APP$^+$ spheroids observed by immunofluorescence staining, this aspect was never proven experimentally. During tissue embedding, the true volumes of cells and cellular processes can change. To directly compare axonal swellings on the ultrastructural and histological level, first, the cell nuclei were reconstructed from confocal immunfluorescence and EM images and the volume of cell nuclei was measured (Fig. 2g, h). The volume of cell nuclei was larger in 3D EM images compared to cell nuclei in confocal immunfluorescence images (Fig. 2i), which could be due to tissue shrinkage or swelling. To correct for these artifacts in the subsequent analysis, the mean volume of cell nuclei of fluorescence images was divided by the mean volume of cell nuclei obtained from EM images, which resulted in a "normalization value" of 0.65. Second, the volume of axonal swellings was measured in consecutive EM images, and compared to the volume of axonal spheroids measured in free-floating brain sections processed for anti-APP immunofluorescence (Fig. 2j, k). To correct for tissue artifacts, values of ultrastructural axonal swellings (3D EM) were multiplied by the normalization value. As demonstrated in Fig. 2l, mean volumes of ultrastructural axonal swellings (26.79 μm^3 ± 7.20 μm^3) did not significantly differ from mean volumes of APP$^+$ spheroids (31.32 μm^3 ± 2.43 μm^3) after correcting for tissue shrinkage or swelling artifacts.

Vesicular and Mitochondrial Proteins Accumulate as Spheroids

At higher resolution, it was evident that axonal swellings contained large numbers of two distinct densely packed structures, namely, (i) synaptic vesicles and (ii) mitochondria (Fig. 2f). Next, we wanted to analyze whether mitochondria, trapped in axonal swellings, can as well be visualized by immunohistochemistry. Furthermore, we asked whether synaptic vesicles, as observed by 3D EM, contain other synaptic proteins than APP. First, slides were processed for anti-VGLUT1 immunohistochemistry because the vast majority of cortical neurons are excitatory ones and release the excitatory transmitter glutamate. In the gray matter (i.e., cortex) of control and cuprizone-treated mice, VGLUT1 was

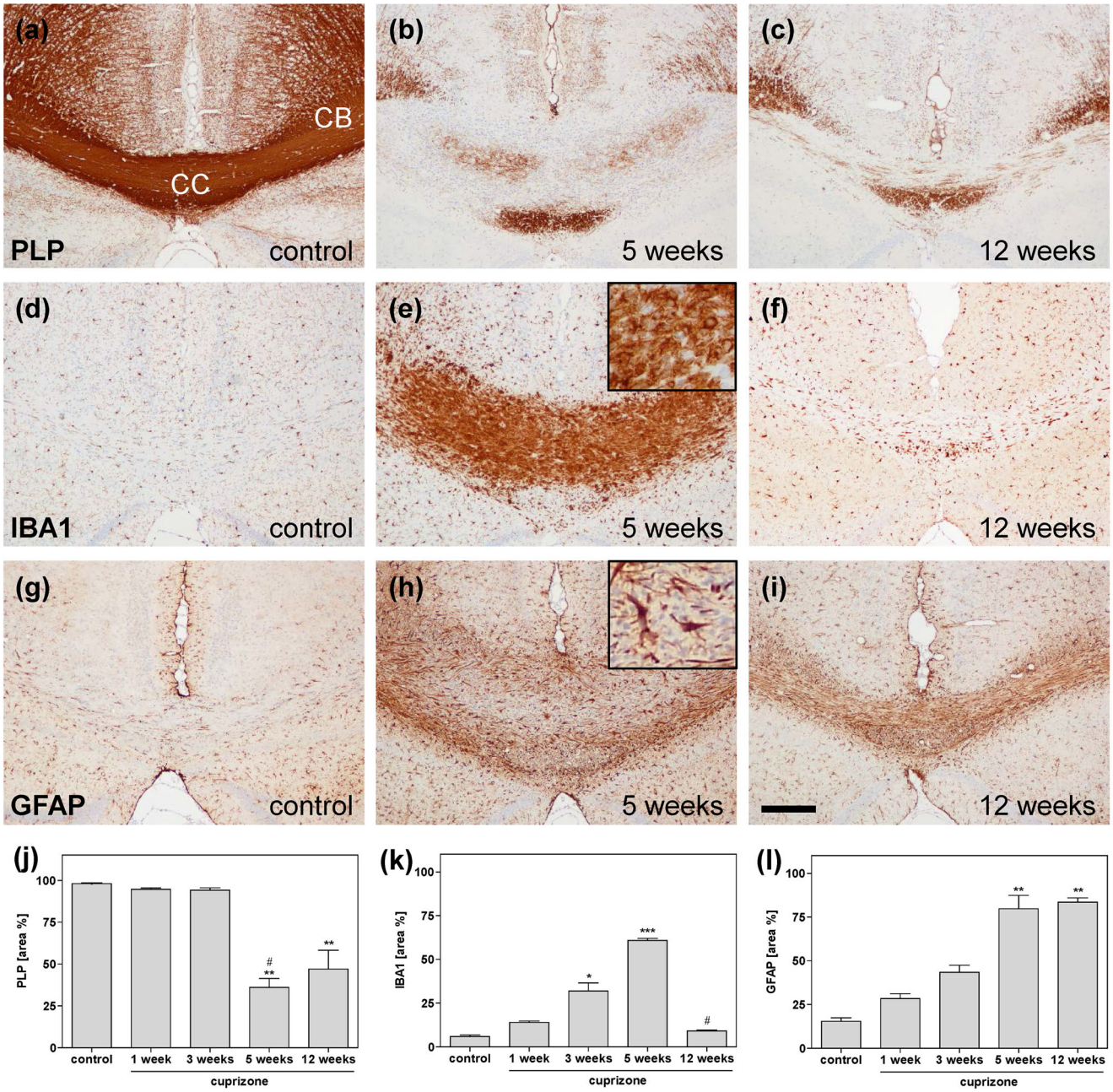

Fig. 1 Immunohistochemical analysis of myelin and glial activation during cuprizone intoxication. Representative sections illustrate immunohistochemical staining for PLP, IBA1, and GFAP in the midline of the corpus callosum (CC) including the cingulum bundle (CB) of controls (**a**, **d**, **g**) and after acute (**b**, **e**, **h**) and chronic demyelination (**c**, **f**, **i**). Densitometric analysis of anti-PLP (**j**), anti-IBA1 (**k**), and anti-GFAP (**l**) stained sections. Four to five animals per group; one independent experiment. Significant differences are indicated by asterisks (vs controls) and hashtags (vs preceding time point) (*#$p < 0.5$; **##$p < 0.01$; ***###$p < 0.001$). Scale bar = 200 μm

present around neuronal cell bodies what appeared to be excitatory boutons. As one would expect, VGLUT1$^+$ signals appeared as small granular spots (Fig. 3a), indicating specificity of the applied antibody. In the white matter (i.e., CC and CB) of control animals, VGLUT1 was virtually absent (Fig. 3a, d). During cuprizone-induced demyelination, the densities of VGLUT1$^+$ spheroids gradually increased until week 5 (Fig. 3b, d). At week 12, the density of VGLUT1$^+$ spheroids was slightly lower compared to week 5, but the diameter of individual VGLUT1$^+$ spheroids was significantly larger (Fig. 3c–e).

The majority of axons in the CC are glutamatergic. However, there is rising evidence about inhibitory fibers, connecting the two hemispheres [35]. We next examined whether synaptic vesicles, synthesized by inhibitory neurons, as well accumulate in the demyelinated CC. The gray matter of control and cuprizone-treated animals displayed a fine granular VGAT$^+$ staining, whereas the white matter of the

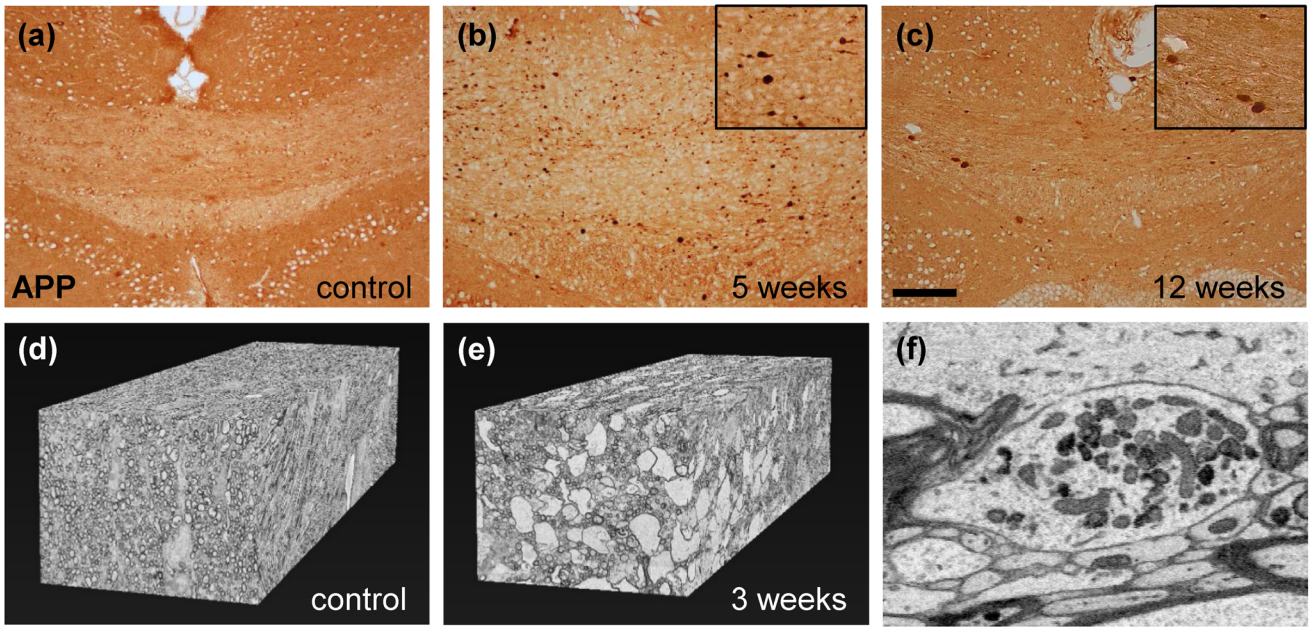

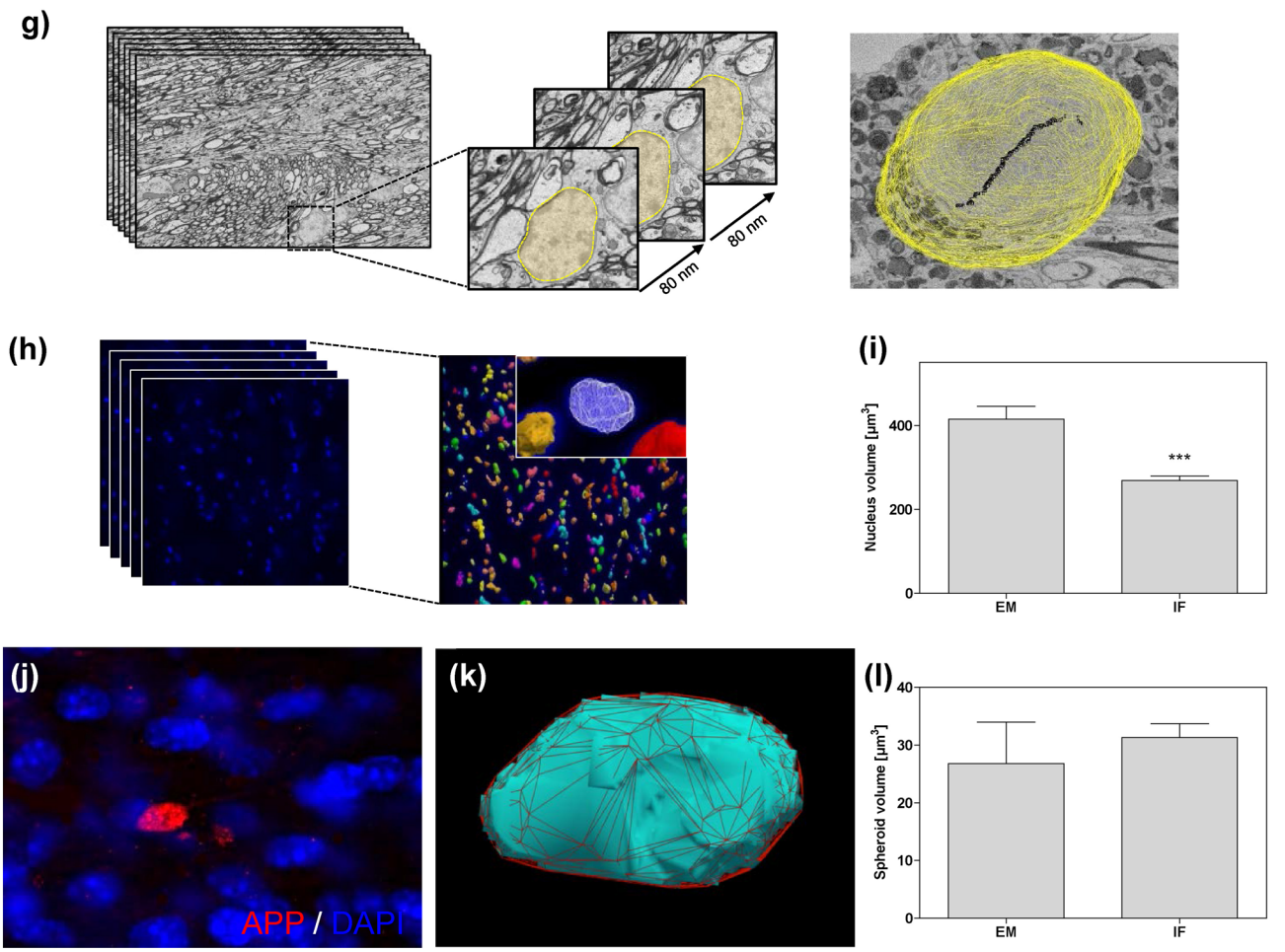

CC was virtually devoid of any VGAT^{+} signal (Fig. 3f). Of note, VGAT did not accumulate as spheroids during cuprizone-induced demyelination (Fig. 3g, h).

Since we observed accumulation of mitochondria in axonal swellings on the ultrastructural level, we next looked for the localization of mitochondrial proteins by immunohistochemistry.

◀ **Fig. 2** Immunohistochemical and ultrastructural analysis of axonal damage. Representative sections illustrate immunohistochemical staining for amyloid precursor protein (APP) in the midline of the corpus callosum in controls (**a**), after acute (**b**) and chronic (**c**) demyelination. Three-dimensional (3D) reconstructions of 3D electron microscopy (EM) images of the CC of control (**d**) and 3 weeks cuprizone-treated animals (**e**). The EM image shows a focal axonal swelling filled with mitochondria and synaptic vesicles in the CC of cuprizone-fed mice (**f**). Cell nuclei in EM images were reconstructed by tracing their outlines using ImageJ (**g**). Cell nuclei in APP-immunfluorescence (IF) images were reconstructed using Neurolucida360 (**h**). Volume of cell nuclei in EM and APP-IF images (**i**). Representative image and reconstruction of an APP^+ spheroid (**j**, **k**). Spheroid volume of 3D EM and APP-IF images after correction of tissue shrinkage or swelling artifacts (**l**). Four animals per group; one independent experiment. Statistically significant differences are indicated by asterisks (***###$p < 0.001$). Scale bar = 100 μm (**a**–**c**)

COX4 is located in the inner mitochondrial membrane, while VDAC1, also known as mitochondrial porin, is a channel of the outer mitochondrial membrane, respectively. Both were strongly expressed in the gray matter of control animals. VDAC1 and COX4 signals appeared as fine granular spots within the neuropil, along with a stronger cytoplasmic staining (Fig. 4a, d). In contrast, the white matter was virtually devoid of $VDAC1^+$ and $COX4^+$ signals (Fig. 4a, d), at least at the applied antibody concentrations. During demyelination, $VDAC1^+$ and $COX4^+$ spheroids densities increased till week 5 (Fig. 4b, e, g, h). Such relatively big $VDAC1^+$ and $COX4^+$ spheroids were not in a spatial relation to cell nuclei. Of note, at week 5, we observed as well high densities of small $COX4^+$ and $VDAC1^+$ dots, which were frequently found in close proximity to a nucleus. These

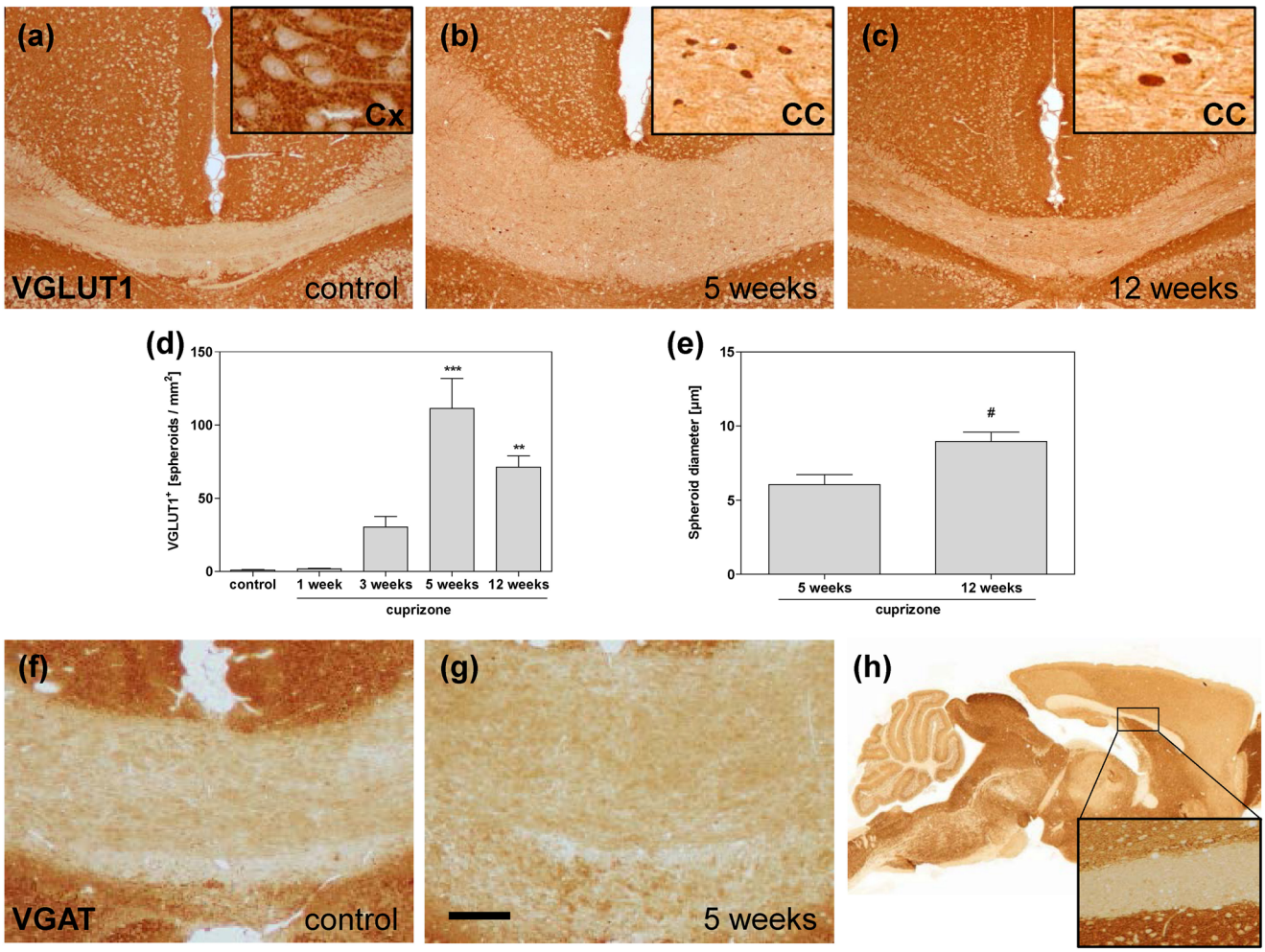

Fig. 3 Immunohistochemical analysis of vesicular proteins. Representative sections illustrate immunohistochemical staining for VGLUT1 in the cortex (Cx) and corpus callosum (CC) of control animals (**a**), after acute (**b**) and chronic demyelination (**c**). Insets show higher magnification of VGLUT1 in the Cx and the CC. Quantification of $VGLUT1^+$ spheroids during cuprizone-induced demyelination (**d**). Spheroid diameter after acute and chronic demyelination (**e**). Representative images show VGAT immunohistochemistry in controls (**f**) and coronal and sagittal sections of cuprizone-intoxicated mice (**g**, **h**). Five to seven animals per group; two independent experiments. Statistically significant differences are indicated by asterisks (vs controls) and hashtags (vs preceding time point) (*#$p < 0.5$; ***###$p < 0.001$). Scale bar = 200 μm (**a**–**c**); 100 μm (**f**, **g**)

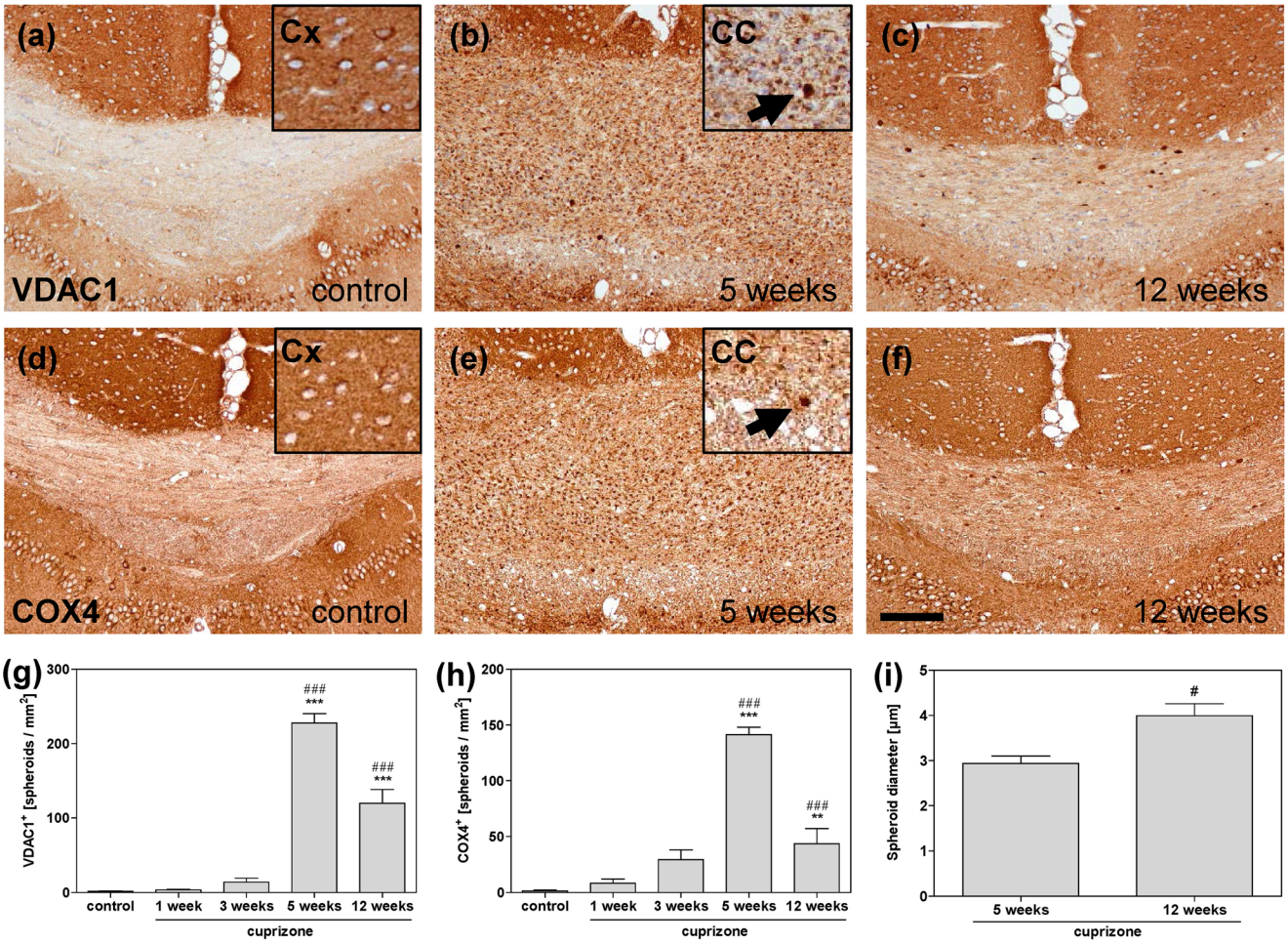

Fig. 4 Immunohistochemical analysis of mitochondrial proteins. Representative sections illustrate immunohistochemical staining for VDAC1 and COX4 in the corpus callosum (CC) of controls (**a**, **d**) and during acute (**b**, **e**) and chronic demyelination (**c**, **f**). Insets show higher magnification of VDAC1 and COX4 in the cortex (Cx) and CC. Quantification of VDAC1$^+$ (**g**) and COX4$^+$ (**h**) spheroids after cuprizone-induced demyelination. COX4$^+$ spheroids increased in size during cuprizone-induced demyelination (**i**). Five to nine animals per group; two independent experiments. Statistically significant differences are indicated by asterisks (vs controls) and hashtags (vs preceding time point) (*#$p < 0.5$; **##$p < 0.01$; ***###$p < 0.001$). Scale bar = 100 µm

small dots probably represent mitochondria in activated microglia and/or astrocytes. At week 12, densities of VDAC1$^+$ and COX4$^+$ spheroids were decreased, while the spheroid size was increased compared to week 5 (Fig. 4c, f–i). Beyond, the fine-grained, perinuclear staining pattern was robustly reduced at week 12, further indicating that this fine staining pattern reflects microglial mitochondria rather than mitochondria within axonal spheroids.

Vesicular and Mitochondrial Spheroids Serve as Marker for Axonal Damage

To verify VGLUT1 as a marker for axonal injury, we performed co-localization studies for VGLUT1 and APP. VGLUT1/APP double staining revealed co-localization of VGLUT1$^+$ and APP$^+$ spheroids after acute and chronic demyelination (Fig. 5a–f). Around one quarter of spheroids were VGLUT1$^+$/APP$^+$ after 5 weeks of cuprizone treatment, shifting to one third of spheroids at the 12-week time point. VGLUT1$^-$/APP$^+$ spheroids comprised the majority of spheroids at both time points, ranging from 64% (acute demyelination) to 49% (chronic demyelination), whereas just some axonal spheroids were VGLUT1 single positive (Fig.5g).

It has been suggested that VGLUT1 is expressed in synaptic-like microvesicles of astrocytes [23, 36, 37]. We were, thus, next interested whether VGLUT1 single positive spheroids belong to the astrocyte population. To investigate this, we first performed immunofluorescence double staining experiments with anti-VGLUT1 and anti-GFAP antibodies. As shown, VGLUT1 did not co-localize with GFAP$^+$ astro-

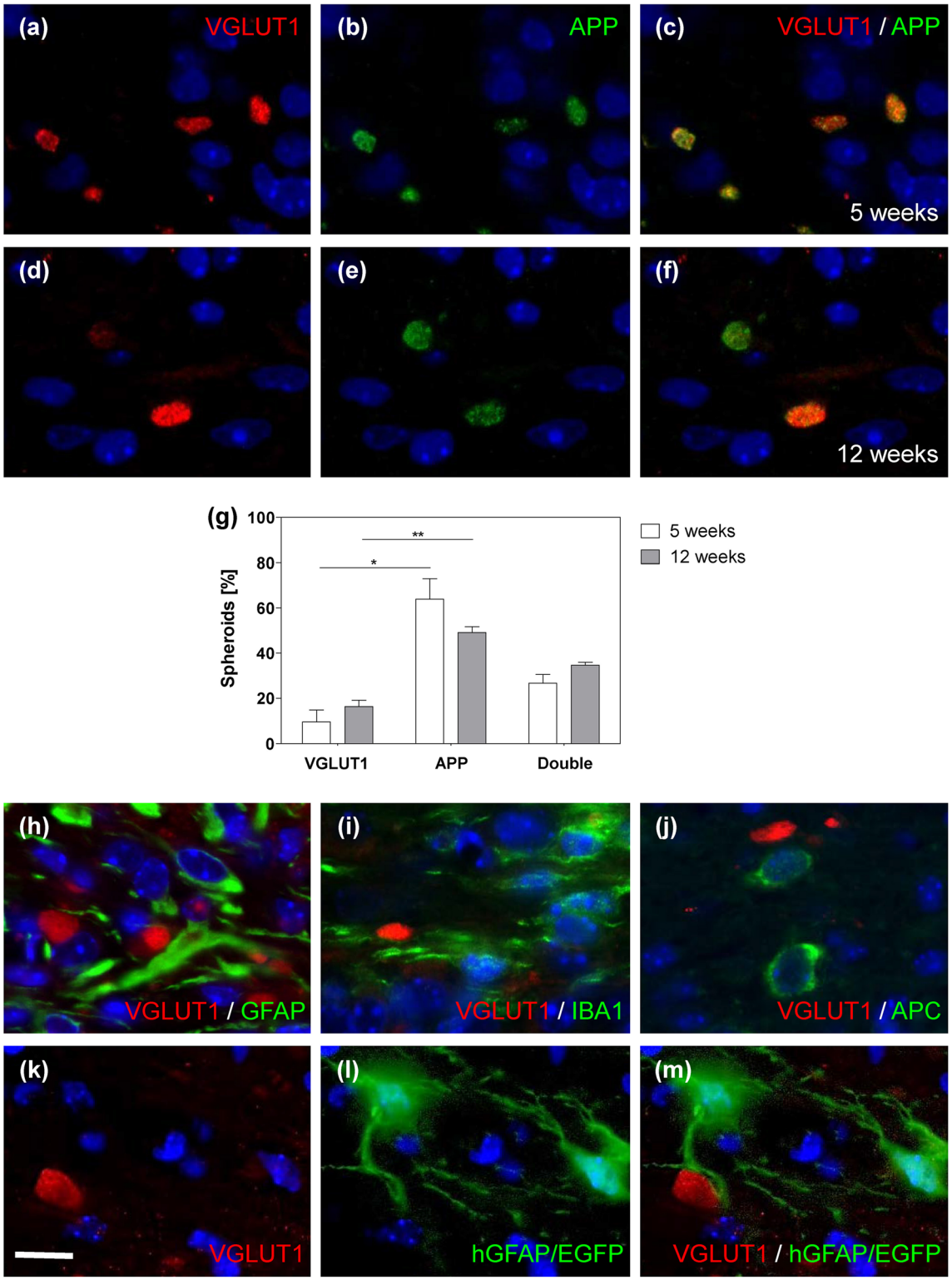

Fig. 5 VGLUT as a marker for axonal damage. VGLUT1 and APP co-localize in the corpus callosum during acute (**a**–**c**) and chronic demyelination (**d**–**f**). Quantification of APP^+, $VGLUT1^+$, and $APP^+/VGLUT1^+$ spheroids (**g**). VGLUT1 does not co-localize with the astrocytic marker GFAP (**h**), the microglial marker IBA1 (**i**), or the oligodendroglial marker APC (**j**). VGLUT1 also does not co-localize with hGFAP $EGFP^+$ astrocytes (**k**–**m**). Three to five animals per group; one independent experiment. Statistically significant differences are indicated by asterisks (**$p < 0.01$; **$p < 0.01$). Scale bar = 10 μm

cytes in the CC (Fig. 5h). To further confirm this result, we performed anti-VGLUT1 immunofluorescence staining in hGFAP-EGFP-mice. These mice express GFAP not only in proximal processes, but also in fine distal processes of astrocytes [30]. In line with our results obtained by fluorescence-double labeling, we did not find any co-localization of VGLUT1 and GFAP in the CC (Fig. 5k–m). Furthermore, VGLUT1 did neither co-localize with IBA1$^+$ microglia nor APC$^+$ mature oligodendrocytes in the CC (Fig. 5i, j). In summary, this series of experiments suggests that VGLUT1 accumulates in injured axons.

Next, we investigated whether co-localization of vesicles and mitochondria, as evident on the ultrastructural level, could also be observed by immunohistochemistry. Co-localization of APP and COX4 was found in the CC after acute and chronic demyelination (Fig. 6a–f). Comparable to our results obtained by VGLUT1/APP double labeling, COX4$^-$/APP$^+$ spheroids were more numerous than COX4$^+$/APP$^+$ spheroids (Fig. 6g). Mitochondria are found in the cytoplasm of almost all eukaryotic cells. In order to confirm that COX4 single positive spheroids represent axonal accumulations, immunofluorescence double stains for COX4 and glia cell markers were performed. COX4$^+$ spheroids did neither co-localize with GFAP$^+$ astrocytes, IBA1$^+$microglia, nor APC$^+$ mature oligodendrocytes (Fig. 6h–j). However, perinuclear COX4 signal was detected in IBA1 positive microglia in the CC of cuprizone-treated animals (Fig. 6i). This suggests that small COX4$^+$ spots represent mitochondria of glial cells, while structures without nuclear staining represent axonal accumulations.

Finally, we compared the sensitivity of APP, VGLUT1, VDAC1, and COX4 as markers for axonal injury during acute and chronic demyelination. In acute lesions, numbers of VGLUT1$^+$, VDAC1$^+$, and COX4$^+$ spheroids were significantly lower compared to APP$^+$ spheroids (Fig. 7a; Table 1). After chronic demyelination, numbers of spheroids were similar for VGLUT1 and COX4, while numbers of VDAC1$^+$ spheroids tended to be higher (Fig. 7b). These data indicate that APP is, among the analyzed proteins, the most sensitive marker for axonal transport disturbances after acute demyelination, while this is not the case after chronic demyelination.

Vesicular and Mitochondrial Proteins Accumulate as Spheroids in MS Lesions

Chronic active lesions were demyelinated and hypocellular with accumulations of macrophages/microglia at the lesion border (Fig. 8a, b). To analyze whether acute axonal damage is present in chronic active MS lesions, consecutive sections were stained for APP. In affected white matter areas, numerous APP$^+$ spheroids were found in the center and border of the lesion (Fig. 8c). To verify whether lesions as well contain VGLUT1$^+$ and COX4$^+$ spheroids, we next performed immunohistochemistry for VGLUT1 and COX4. Both, VGLUT1$^+$ and COX4$^+$ spheroids were found in the affected white matter (Fig. 8d, e), while the normal appearing white matter was virtually devoid of spheroids positive for VGLUT1 and COX4. As expected, perinuclear COX4$^+$ staining was regularly seen in lesions and non-lesion areas. Additionally, VGLUT1$^+$ glial-like structures could be observed in lesions and the surrounding tissue (not shown). To confirm that VGLUT1$^+$ spheroids resemble axonal damage in human MS lesions, we performed co-localization studies of VGLUT1 and APP. The vast majority of spheroids were positive for APP, while just a minor number of spheroids was VGLUT1$^+$/APP$^+$ (Fig. 8f–h).

Discussion

Organelle and vesicle transport is vital for the maintenance of axonal health, in which the distances between sites of organelle biogenesis, function, and recycling or degradation can be vast. To better understand the signature of axonal transport deficits and damage, we selectively investigated vesicular and mitochondrial transport deficits, and compared ultrastructural and histological morphologies.

We first determined the level of axonal damage in the cuprizone model using anti-APP immunohistochemistry, which is a standard method for detecting axonal transport deficits and, hence, acute axonal injury [4, 13, 14, 38]. In line with previous results, we observed accumulation of APP after acute and chronic cuprizone-induced demyelination [15, 20]. Accumulations of APP have also been observed in other MS animal models including experimental autoimmune encephalomyelitis (EAE) and the lysophosphatidylcholine-induced demyelination model [15, 39]. Findings from EAE experiments suggest that alterations in axonal transport is an early event and not simply the consequence of disease progression [40].

To determine whether APP$^+$ spheroids represent axonal swellings observed on the ultrastructural level, we first compared the volumes of axonal spheroids/swellings using two different methods (i.e., confocal anti-APP immunofluorescence stains and 3D EM). For most studies exploring axonal damage, either one or the other method was used [14, 27]. To the best of our knowledge, this is the first study comparing both methods site by site. Therefore, tissue of 3 weeks cuprizone intoxication was used since intoxication with cuprizone for 5 weeks results in severe demyelination and tissue damage. After 3 weeks, the CC is only partly demyelinated, the morphology is largely preserved, and axonal swellings can be clearly identified. During tissue embedding, the true volumes of cells and cellular processes can change because of tissue shrinkage or swelling, respectively.

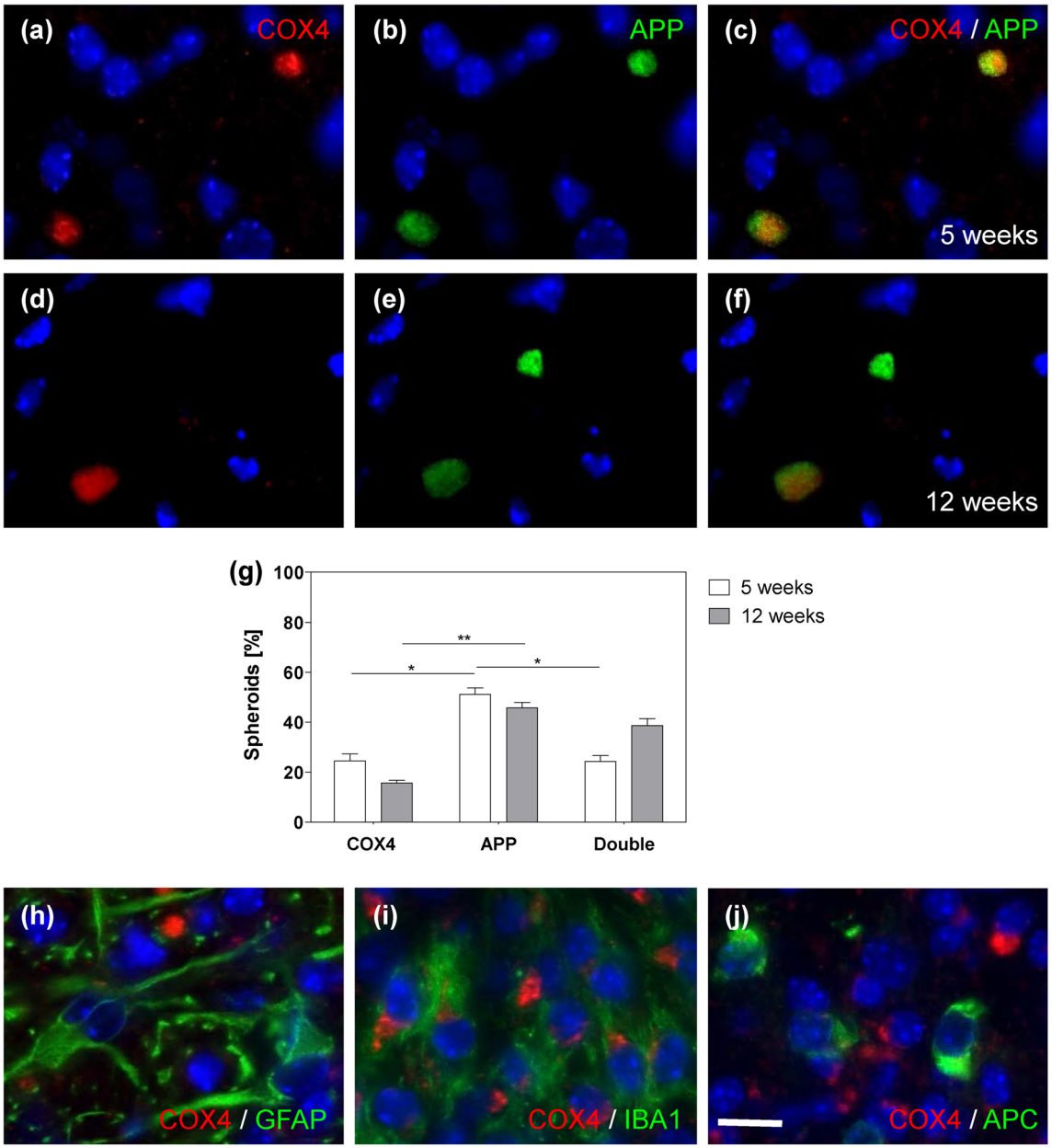

Fig. 6 COX4 as a marker for axonal damage. COX4 and APP co-localize in the corpus callosum during acute (**a**–**c**) and chronic demyelination (**d**–**f**). Quantification of APP^+, $COX4^+$, and $APP^+/COX4^+$spheroids (**g**). $COX4^+$ spheroids do not co-localize with the astrocytic marker GFAP (**h**), microglial marker IBA1 (**i**), or the oligodendroglial marker APC (**j**). Perinuclear COX4 co-localizes with the microglial marker IBA1 (**i**). Five animals per group; one independent experiment. Statistically significant differences are indicated by asterisks (*$p < 0.05$, **$p < 0.01$). Scale bar = 10 μm

To account for different extends of shrinkage or swelling artifacts in our differentially processed tissues (i.e., immunofluorescence versus 3D EM), we first measured the volume of cell nuclei in both approaches and thereby determined a "normalization value." Then, we quantified volumes of anti-APP^+ spheroids in free-floating sections and compared them to volumes of axonal swellings quantified in 3D EM images. As demonstrated in our studies, the mean spheroids volumes were not different from mean axonal swelling volumes if we accounted for tissue artifacts.

3D EM can be considered as gold standard method to detect axonal damage in our days. Using this method, whole axons can be tracked and reconstructed and any anomaly including axonal swellings can be made visible [27]. Furthermore, densely packed vesicles and mitochondria can be demonstrated in axonal swellings. In line with this, Ohno and colleagues showed in EM images axonal swellings filled with densely packed membranous organelles, including mitochondria [27]. Thus, the identification and localization of ultrastructural changes using 3D EM

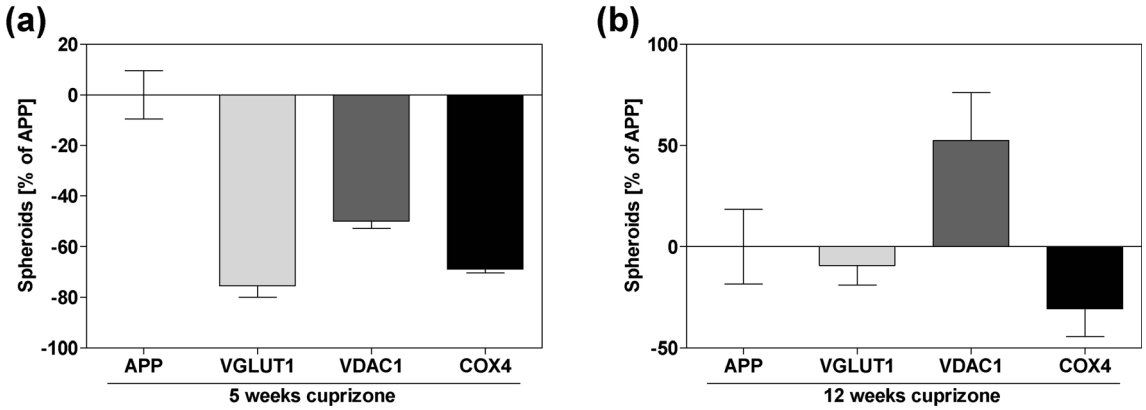

Fig. 7 Graphs show the ratio of VGLUT1$^+$, VDAC1$^+$ or COX4$^+$ spheroids in relation to APP$^+$ spheroids during acute (**a**) and chronic (**b**) demyelination

provides valuable information. However, EM images provide no information about individual vesicles and their contents. Immunohistochemistry is needed to characterize the accumulated vesicles and organelles on the biochemical level. Thus, the combination of immunohistochemistry and 3D EM provides a powerful tool to study the extent and signature of acute axonal injury. By means of immunohistochemistry, we could show that different vesicular (APP and VGLUT1) as well as mitochondrial (VDAC1 and COX4) proteins accumulate as axonal spheroids. In line with accumulation of APP$^+$ spheroids, densities of vesicular and mitochondrial spheroids was most intense in areas of intense microgliosis. Previous studies report organelle accumulations before obvious demyelination [7, 40]. This indicates a complex pathomechanism, which is not simply a direct consequence of demyelination. Data from previous studies suggest a strong correlation between microglia/macrophages activation and axonal transport deficits [7], which we could also observe in our study.

Interestingly, we observed high densities of small vesicular and mitochondrial spheroids during acute demyelination, while we found less, but larger spheroids during chronic demyelination. Increased spheroid diameters are likely caused by the accumulation of more cargos at the side of permanent axonal damage. Another explanation would be that smaller axons are affected during acute demyelination, while larger axons may be involved during the chronic phase. Using in vivo imaging, it has been shown that axonal transport deficits are reversible [41]. At the beginning, spheroids appear to be a temporary event, not caused by destruction of the microtubules and its components. It might be possible that cargos transiently "lose" their connection to binding proteins and microtubules under acute injury conditions and later find back to their destination. Thus, it was proposed by Gudi and colleagues that large spheroids represent permanent axonal damage, while smaller spheroids might represent reversible transport deficits [7]. It would now be interesting to systematically analyze the molecular composition of large versus small axonal spheroids by, for example, immunogold labeling experiments or, as performed in this study, immunofluorescence.

Another important observation in this study is the absence of VGAT$^+$ spheroids in the demyelinated CC. It has been suggested that GABAergic as well as glutamatergic neurons send their axons through the CC [35]. We were initially surprised that damaged axons were not labeled with VGAT. The fact that VGAT immunoreactivity is found only in terminal regions in the cortex and not in damaged axons may mean that (i) axons of inhibitory neurons or the specific transport mechanism of VGAT$^+$ vesicles are not affected or that (ii) relatively small numbers of vesicles filled with VGAT are transported along the axons. Thus, the small amount of accumulated VGAT might be beneath the immunohistochemical detection limit. The latter seems more likely, since loss and damage of GABAergic interneurons have been previously shown [42–44]. In this study, we further showed not only vesicular but also mitochondrial accumulations. Mitochondria play a pivotal role in homeostasis and function of neurons

Table 1 Details of the statistical analysis of spheroid counts during active (5 weeks) and chronic demyelination (12 weeks). ***$p < 0.001$

	5 weeks (mean ± SEM)	p (vs APP)	12 weeks (mean ± SEM)	p (vs APP)	% of 5 weeks
APP/mm^2	454.3 ± 43.4	–	78.4 ± 14.5	–	17.3
VGLUT1/mm^2	111.3 ± 20.5	***	71.2 ± 7.6	ns	64.0
VDAC1/mm^2	227.7 ± 12.5	***	119.6 ± 18.7	ns	52.5
COX4/mm^2	141.4 ± 6.7	***	54.3 ± 10.8	ns	38.4

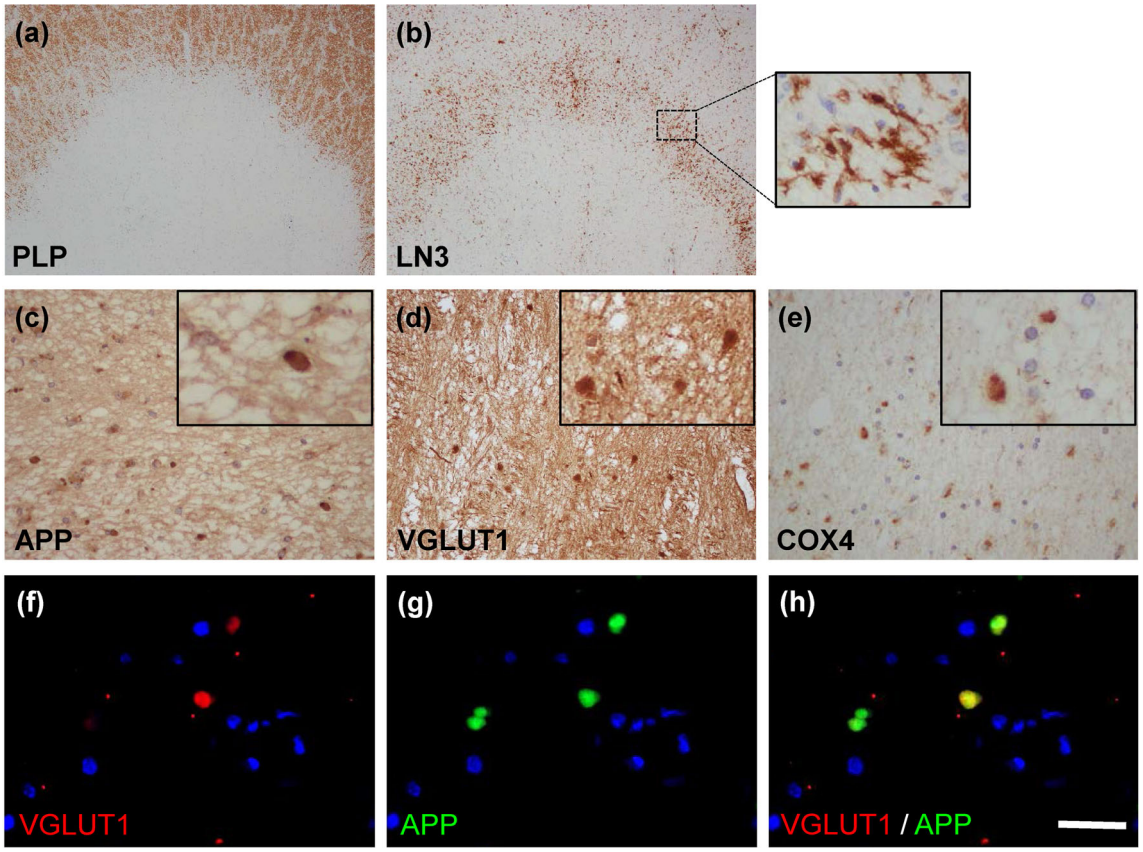

Fig. 8 Representative images show the extent of demyelination (PLP) (**a**) and inflammation (LN3, MHC-II to visualize antigen-presenting cells) (**b**) in a chronic active MS lesion. Representative images for APP$^+$ (**c**), VGLUT1$^+$ (**d**), and COX4$^+$ (**e**) spheroids in chronic active MS lesions. Co-localization of APP and VGLUT1 (**f**–**h**). Scale bar = 580 μm (**a**, **b**); 10 μm (**c**–**e**); 25 μm (**f**–**h**)

and increasing evidence suggests that dysfunction of axonal mitochondria and mitochondrial transport are implicated in degeneration of axons [45, 46]. Disturbed transport and accumulation of mitochondria may cause local energy depletion and changes in calcium buffering. Furthermore, dysfunctional mitochondria may release reactive oxygen species that lead to increased axon vulnerability [47]. Studies in EAE mice have described axonal accumulation of COX4$^+$ mitochondria in correlation with axonal degeneration [48]. Additionally, swellings of axons and mitochondrial pathology was observed at the side of focal axonal degeneration in EAE and active MS lesions [41]. In the present study, we could also identify COX4$^+$ accumulations at side of axonal damage. Mitochondria are not only important for proper neuronal functioning, but also for glial cells [49]. Here, we found that small COX4$^+$ dots appear in high numbers in activated microglia during acute demyelination. Thus, COX4 may serve not only as a marker for axonal damage, when accumulated as spheroids, but might also represent glial activation. Of note, careful examination of the tissues allow, based on nuclear co-localization, a distinction between mitochondria accumulating in glia cells versus mitochondria accumulating in axonal spheroids.

In summary, the current results demonstrate a vesicular as well as mitochondrial accumulation at sites of acute axonal injury, not only in the cuprizone model, but also in MS lesions. We propose that the combination of 3D EM and immunohistochemistry serves as a valuable tool to study axonal damage in more detail and that specific proteins, including VGLUT1 and COX4, could serve as selective markers for axonal damage. Further studies, especially in autopsy material, are required to ascertain how vesicular and mitochondrial accumulations vary in different types of lesions and different clinical phenotypes. A better understanding of axonal injury might thus contribute to the development of potential treatments which ameliorate or even reverse axonal pathology in MS.

Acknowledgments We thank Christiane Nolte and Helmut Kettenmann for providing hGFAP/EGFP transgenic mice (Max-Delbrueck Center for Molecular Medicine in the Helmholtz Association, Berlin, Germany). We thank Sarah Wübbel, Astrid Baltruschat, and Beate Aschauer for their excellent and valuable technical assistance.

Compliance with Ethical Standards

Conflict of Interest The authors declare that they have no conflict of interest.

References

1. Lublin FD, Reingold SC (1996) Defining the clinical course of multiple sclerosis: results of an international survey. National Multiple Sclerosis Society (USA) Advisory Committee on Clinical Trials of New Agents in Multiple Sclerosis. Neurology 46(4):907–911
2. Kipp M, Nyamoya S, Hochstrasser T, Amor S (2017) Multiple sclerosis animal models: a clinical and histopathological perspective. Brain Pathol (Zurich, Switzerland) 27(2):123–137. https://doi.org/10.1111/bpa.12454
3. Hochstrasser T, Jiangshan Z, Ruhling S, Schmitz C, Kipp M (2018) Do pre-clinical multiple sclerosis models allow us to measure neurodegeneration and clinical progression? Expert Rev Neurother 18:1–3. https://doi.org/10.1080/14737175.2018.1459190
4. Kuhlmann T, Lingfeld G, Bitsch A, Schuchardt J, Bruck W (2002) Acute axonal damage in multiple sclerosis is most extensive in early disease stages and decreases over time. Brain J Neurol 125(Pt 10):2202–2212
5. Schirmer L, Antel JP, Bruck W, Stadelmann C (2011) Axonal loss and neurofilament phosphorylation changes accompany lesion development and clinical progression in multiple sclerosis. Brain Pathol (Zurich, Switzerland) 21(4):428–440. https://doi.org/10.1111/j.1750-3639.2010.00466.x
6. Trapp BD, Peterson J, Ransohoff RM, Rudick R, Mork S, Bo L (1998) Axonal transection in the lesions of multiple sclerosis. N Engl J Med 338(5):278–285. https://doi.org/10.1056/nejm199801293380502
7. Gudi V, Gai L, Herder V, Tejedor LS, Kipp M, Amor S, Suhs KW, Hansmann F et al (2017) Synaptophysin is a reliable marker for axonal damage. J Neuropathol Exp Neurol 76:109–125. https://doi.org/10.1093/jnen/nlw114
8. Koo EH, Sisodia SS, Archer DR, Martin LJ, Weidemann A, Beyreuther K, Fischer P, Masters CL et al (1990) Precursor of amyloid protein in Alzheimer disease undergoes fast anterograde axonal transport. Proc Natl Acad Sci U S A 87(4):1561–1565
9. Groemer TW, Thiel CS, Holt M, Riedel D, Hua Y, Huve J, Wilhelm BG, Klingauf J (2011) Amyloid precursor protein is trafficked and secreted via synaptic vesicles. PLoS One 6(4):e18754. https://doi.org/10.1371/journal.pone.0018754
10. Tyan SH, Shih AY, Walsh JJ, Maruyama H, Sarsoza F, Ku L, Eggert S, Hof PR et al (2012) Amyloid precursor protein (APP) regulates synaptic structure and function. Mol Cell Neurosci 51(1–2):43–52. https://doi.org/10.1016/j.mcn.2012.07.009
11. Sherriff FE, Bridges LR, Gentleman SM, Sivaloganathan S, Wilson S (1994) Markers of axonal injury in post mortem human brain. Acta Neuropathol 88(5):433–439
12. Stone JR, Singleton RH, Povlishock JT (2000) Antibodies to the C-terminus of the beta-amyloid precursor protein (APP): a site specific marker for the detection of traumatic axonal injury. Brain Res 871(2):288–302
13. Ferguson B, Matyszak MK, Esiri MM, Perry VH (1997) Axonal damage in acute multiple sclerosis lesions. Brain J Neurol 120(Pt 3):393–399
14. Bitsch A, Schuchardt J, Bunkowski S, Kuhlmann T, Bruck W (2000) Acute axonal injury in multiple sclerosis. Correlation with demyelination and inflammation. Brain J Neurol 123(Pt 6):1174–1183
15. Hoflich KM, Beyer C, Clarner T, Schmitz C, Nyamoya S, Kipp M, Hochstrasser T (2016) Acute axonal damage in three different murine models of multiple sclerosis: a comparative approach. Brain Res 1650:125–133. https://doi.org/10.1016/j.brainres.2016.08.048
16. Buschmann JP, Berger K, Awad H, Clarner T, Beyer C, Kipp M (2012) Inflammatory response and chemokine expression in the white matter corpus callosum and gray matter cortex region during cuprizone-induced demyelination. Journal of molecular neuroscience : MN 48(1):66–76. https://doi.org/10.1007/s12031-012-9773-x
17. Kipp M, Clarner T, Dang J, Copray S, Beyer C (2009) The cuprizone animal model: new insights into an old story. Acta Neuropathol 118(6):723–736. https://doi.org/10.1007/s00401-009-0591-3
18. Vana AC, Flint NC, Harwood NE, Le TQ, Fruttiger M, Armstrong RC (2007) Platelet-derived growth factor promotes repair of chronically demyelinated white matter. J Neuropathol Exp Neurol 66(11):975–988. https://doi.org/10.1097/NEN.0b013e3181587d46
19. Mason JL, Langaman C, Morell P, Suzuki K, Matsushima GK (2001) Episodic demyelination and subsequent remyelination within the murine central nervous system: changes in axonal calibre. Neuropathol Appl Neurobiol 27(1):50–58
20. Lindner M, Fokuhl J, Linsmeier F, Trebst C, Stangel M (2009) Chronic toxic demyelination in the central nervous system leads to axonal damage despite remyelination. Neurosci Lett 453(2):120–125. https://doi.org/10.1016/j.neulet.2009.02.004
21. Hennequin G, Agnes EJ, Vogels TP (2017) Inhibitory plasticity: balance, control, and codependence. Annu Rev Neurosci 40:557–579. https://doi.org/10.1146/annurev-neuro-072116-031005
22. Sheng M, Kim MJ (2002) Postsynaptic signaling and plasticity mechanisms. Science (New York, NY) 298(5594):776–780. https://doi.org/10.1126/science.1075333
23. Fremeau RT Jr, Voglmaier S, Seal RP, Edwards RH (2004) VGLUTs define subsets of excitatory neurons and suggest novel roles for glutamate. Trends Neurosci 27(2):98–103. https://doi.org/10.1016/j.tins.2003.11.005
24. McIntire SL, Reimer RJ, Schuske K, Edwards RH, Jorgensen EM (1997) Identification and characterization of the vesicular GABA transporter. Nature 389(6653):870–876. https://doi.org/10.1038/39908
25. Liguz-Lecznar M, Skangiel-Kramska J (2007) Vesicular glutamate transporters (VGLUTs): the three musketeers of glutamatergic system. Acta Neurobiol Exp 67(3):207–218
26. Andrews H, White K, Thomson C, Edgar J, Bates D, Griffiths I, Turnbull D, Nichols P (2006) Increased axonal mitochondrial activity as an adaptation to myelin deficiency in the Shiverer mouse. J Neurosci Res 83(8):1533–1539. https://doi.org/10.1002/jnr.20842
27. Ohno N, Chiang H, Mahad DJ, Kidd GJ, Liu L, Ransohoff RM, Sheng ZH, Komuro H et al (2014) Mitochondrial immobilization mediated by syntaphilin facilitates survival of demyelinated axons. Proc Natl Acad Sci U S A 111(27):9953–9958. https://doi.org/10.1073/pnas.1401155111
28. Han SM, Baig HS, Hammarlund M (2016) Mitochondria localize to injured axons to support regeneration. Neuron 92(6):1308–1323. https://doi.org/10.1016/j.neuron.2016.11.025
29. Karbowski M, Neutzner A (2012) Neurodegeneration as a consequence of failed mitochondrial maintenance. Acta Neuropathol 123(2):157–171. https://doi.org/10.1007/s00401-011-0921-0
30. Nolte C, Matyash M, Pivneva T, Schipke CG, Ohlemeyer C, Hanisch UK, Kirchhoff F, Kettenmann H (2001) GFAP promoter-controlled EGFP-expressing transgenic mice: a tool to visualize astrocytes and astrogliosis in living brain tissue. Glia 33(1):72–86
31. Seewann A, Kooi EJ, Roosendaal SD, Barkhof F, van der Valk P, Geurts JJ (2009) Translating pathology in multiple sclerosis: the combination of postmortem imaging, histopathology and clinical findings. Acta Neurol Scand 119(6):349–355. https://doi.org/10.1111/j.1600-0404.2008.01137.x
32. Wagenknecht N, Becker B, Scheld M, Beyer C, Clarner T, Hochstrasser T, Kipp M (2016) Thalamus degeneration and inflammation in two distinct multiple sclerosis animal models. J Mol Neurosci : MN https://doi.org/10.1007/s12031-016-0790-z, 60, 102, 114

33. Hochstrasser T, Exner GL, Nyamoya S, Schmitz C, Kipp M (2017) Cuprizone-containing pellets are less potent to induce consistent demyelination in the corpus callosum of C57BL/6 mice. Journal of molecular neuroscience : MN 61(4):617–624. https://doi.org/10.1007/s12031-017-0903-3
34. Grosse-Veldmann R, Becker B, Amor S, van der Valk P, Beyer C, Kipp M (2015) Lesion expansion in experimental demyelination animal models and multiple sclerosis lesions. Mol Neurobiol 53:4905–4917. https://doi.org/10.1007/s12035-015-9420-y
35. Rock C, Zurita H, Lebby S, Wilson CJ, Apicella AJ (2018) Cortical circuits of callosal GABAergic neurons. Cerebral cortex (New York, NY : 1991) 28(4):1154–1167. https://doi.org/10.1093/cercor/bhx025
36. Brumovsky PR (2013) VGLUTs in Peripheral Neurons and the Spinal Cord: Time for a Review. ISRN Neurol. https://doi.org/10.1155/2013/829753
37. Ormel L, Stensrud MJ, Bergersen LH, Gundersen V (2012) VGLUT1 is localized in astrocytic processes in several brain regions. Glia 60:229–238. https://doi.org/10.1002/glia.21258
38. Bramlett HM, Kraydieh S, Green EJ, Dietrich WD (1997) Temporal and regional patterns of axonal damage following traumatic brain injury: a beta-amyloid precursor protein immunocytochemical study in rats. J Neuropathol Exp Neurol 56(10):1132–1141
39. Herrero-Herranz E, Pardo LA, Gold R, Linker RA (2008) Pattern of axonal injury in murine myelin oligodendrocyte glycoprotein induced experimental autoimmune encephalomyelitis: implications for multiple sclerosis. Neurobiol Dis 30(2):162–173. https://doi.org/10.1016/j.nbd.2008.01.001
40. Sorbara CD, Wagner NE, Ladwig A, Nikic I, Merkler D, Kleele T, Marinkovic P, Naumann R et al (2014) Pervasive axonal transport deficits in multiple sclerosis models. Neuron 84(6):1183–1190. https://doi.org/10.1016/j.neuron.2014.11.006
41. Nikic I, Merkler D, Sorbara C, Brinkoetter M, Kreutzfeldt M, Bareyre FM, Bruck W, Bishop D et al (2011) A reversible form of axon damage in experimental autoimmune encephalomyelitis and multiple sclerosis. Nat Med 17(4):495–499. https://doi.org/10.1038/nm.2324
42. Lapato AS, Szu J, Hasselmann JP, Khalaj AJ, Binder DK, Tiwari-Woodruff SK (2017) Chronic demyelination-induced seizures. Neuroscience 346:409–422. https://doi.org/10.1016/j.neuroscience.2017.01.035
43. Rossi S, Muzio L, De Chiara V, Grasselli G, Musella A, Musumeci G, Mandolesi G, De Ceglia R et al (2011) Impaired striatal GABA transmission in experimental autoimmune encephalomyelitis. Brain Behav Immun 25(5):947–956. https://doi.org/10.1016/j.bbi.2010.10.004
44. Falco A, Pennucci R, Brambilla E, de Curtis I (2014) Reduction in parvalbumin-positive interneurons and inhibitory input in the cortex of mice with experimental autoimmune encephalomyelitis. Exp Brain Res 232(7):2439–2449. https://doi.org/10.1007/s00221-014-3944-7
45. Sheng ZH, Cai Q (2012) Mitochondrial transport in neurons: impact on synaptic homeostasis and neurodegeneration. Nat Rev Neurosci 13(2):77–93. https://doi.org/10.1038/nrn3156
46. Lin MT, Beal MF (2006) Mitochondrial dysfunction and oxidative stress in neurodegenerative diseases. Nature 443(7113):787–795. https://doi.org/10.1038/nature05292
47. Baltan S (2014) Excitotoxicity and mitochondrial dysfunction underlie age-dependent ischemic white matter injury. Advances in neurobiology 11:151–170. https://doi.org/10.1007/978-3-319-08894-5_8
48. Bando Y, Nomura T, Bochimoto H, Murakami K, Tanaka T, Watanabe T, Yoshida S (2015) Abnormal morphology of myelin and axon pathology in murine models of multiple sclerosis. Neurochem Int 81:16–27. https://doi.org/10.1016/j.neuint.2015.01.002
49. Rose J, Brian C, Woods J, Pappa A, Panayiotidis MI, Powers R, Franco R (2017) Mitochondrial dysfunction in glial cells: implications for neuronal homeostasis and survival. Toxicology 391:109–115. https://doi.org/10.1016/j.tox.2017.06.011